

# **DEVELOPMENT OF A TORQUE SENSOR- BASED TEST BED FOR ATTITUDE CONTROL SYSTEM VERIFICATION AND VALIDATION**

**Norman Fitz-Coy**

**University of Florida  
Division of Sponsored Research  
207 Ginter Hall  
Gainesville, FL 32611-0001**

**30 December 2017**

**Final Report**

**APPROVED FOR PUBLIC RELEASE; DISTRIBUTION IS UNLIMITED.**



**AIR FORCE RESEARCH LABORATORY  
Space Vehicles Directorate  
3550 Aberdeen Ave SE  
AIR FORCE MATERIEL COMMAND  
KIRTLAND AIR FORCE BASE, NM 87117-5776**

# **DTIC COPY**

## **NOTICE AND SIGNATURE PAGE**

Using Government drawings, specifications, or other data included in this document for any purpose other than Government procurement does not in any way obligate the U.S. Government. The fact that the Government formulated or supplied the drawings, specifications, or other data does not license the holder or any other person or corporation; or convey any rights or permission to manufacture, use, or sell any patented invention that may relate to them.

This report is the result of contracted fundamental research which is exempt from public affairs security and policy review in accordance with AFI 61-201, paragraph 2.3.5.1. This report is available to the general public, including foreign nationals. Copies may be obtained from the Defense Technical Information Center (DTIC) (<http://www.dtic.mil>).

AFRL-RV-PS-TR-2018-0008 HAS BEEN REVIEWED AND IS APPROVED FOR PUBLICATION IN ACCORDANCE WITH ASSIGNED DISTRIBUTION STATEMENT.

//SIGNED//

---

JOSUE D. MUNOZ, DR-II,  
Program Manager

//SIGNED//

---

FRANK R. CHAVEZ, DR-III,  
Deputy, Integrated Experiments  
& Evaluation Division

This report is published in the interest of scientific and technical information exchange, and its publication does not constitute the Government's approval or disapproval of its ideas or findings.

REPORT DOCUMENTATION PAGE				Form Approved OMB No. 0704-0188	
Public reporting burden for this collection of information is estimated to average 1 hour per response, including the time for reviewing instructions, searching existing data sources, gathering and maintaining the data needed, and completing and reviewing this collection of information. Send comments regarding this burden estimate or any other aspect of this collection of information, including suggestions for reducing this burden to Department of Defense, Washington Headquarters Services, Directorate for Information Operations and Reports (0704-0188), 1215 Jefferson Davis Highway, Suite 1204, Arlington, VA 22202-4302. Respondents should be aware that notwithstanding any other provision of law, no person shall be subject to any penalty for failing to comply with a collection of information if it does not display a currently valid OMB control number. <b>PLEASE DO NOT RETURN YOUR FORM TO THE ABOVE ADDRESS.</b>					
1. REPORT DATE (DD-MM-YYYY) 30-12-2017		2. REPORT TYPE Final Report		3. DATES COVERED (From - To) 29 Apr 2015 - 29 Aug 2017	
4. TITLE AND SUBTITLE  Development of a Torque Sensor-Based Test Bed for Attitude Control System Verification & Validation				5a. CONTRACT NUMBER FA9453-15-1-0315	
				5b. GRANT NUMBER	
				5c. PROGRAM ELEMENT NUMBER 62601F	
6. AUTHOR(S) Norman Fitz-Coy				5d. PROJECT NUMBER 4846	
				5e. TASK NUMBER PPM00015968	
				5f. WORK UNIT NUMBER EF125135	
7. PERFORMING ORGANIZATION NAME(S) AND ADDRESS(ES) University of Florida Division of Sponsored Research 207 Grinter Hall Gainesville, FL 32611-0001				8. PERFORMING ORGANIZATION REPORT NUMBER	
9. SPONSORING / MONITORING AGENCY NAME(S) AND ADDRESS(ES) Air Force Research Laboratory Space Vehicles Directorate 3550 Aberdeen Avenue SE Kirtland AFB, NM 87117-5776				10. SPONSOR/MONITOR'S ACRONYM(S) AFRL/RVES	
				11. SPONSOR/MONITOR'S REPORT NUMBER(S) AFRL-RV-PS-TR-2018-0008	
12. DISTRIBUTION / AVAILABILITY STATEMENT Approved for public release; distribution is unlimited.					
13. SUPPLEMENTARY NOTES					
14. ABSTRACT This project covers the development of a torque sensor for verification and validation (V&V) of spacecraft attitude control actuators. The developed sensor directly measures the actuator's output torques using highly accurate laser displacement sensors. Existing V&V approaches are based on spherical air bearing simulators which (1) have limited range of motion about two axes (pitch and roll), (2) are unable to test in a vacuum, and (3) infer determine the actuator's performance through inference rather than direct measurement. This developed sensor overcomes these challenges existing V&V testbeds, thus enabling hardware-in-the-loop tests in realistic environments (i.e., vacuum) and testing of large angle maneuvers. The prototyped sensor is capable of actuators up to 10x10x10 cm in size, but the design is scalable and can be used for any size spacecraft attitude actuator.					
15. SUBJECT TERMS Torque Sensor for Spacecraft Attitude Control Testbed, Verification and Validation, Attitude Control System					
16. SECURITY CLASSIFICATION OF:			17. LIMITATION OF ABSTRACT  SAR	18. NUMBER OF PAGES  40	19a. NAME OF RESPONSIBLE PERSON Josue Munoz
a. REPORT UNCL	b. ABSTRACT UNCL	c. THIS PAGE UNCL			19b. TELEPHONE NUMBER (include area code)

This page is intentionally left blank.

## TABLE OF CONTENTS

List of Figures.....	ii
List of Tables.....	iii
1. SUMMARY .....	1
2. INTRODUCTION .....	1
3. METHODS, ASSUMPTIONS, and PROCEDURES.....	2
3.1. Goals and Objectives .....	2
3.2. Initial Test Mechanism .....	3
3.3. Testbed Development .....	4
3.3.1. Precision Shaft Diameter Selection .....	6
3.3.2. Testbed Stress Analysis .....	8
3.4. Testbed Frequency Analysis .....	13
3.5. Testbed Frequency Test .....	14
3.6. Testbed Calibration .....	15
3.6.1. Calibration process .....	15
3.6.2. Calibration Results .....	17
3.7. Actuator testing .....	19
3.8. Graphical User Interface (GUI).....	27
4. CONCLUSION.....	29
REFERENCES.....	30

## LIST OF FIGURES

Figure 1. Schematic of Hardware-in-the-Loop.....	3
Figure 2. Schematic of test mechanism assembly .....	3
Figure 3. Load applied to the test mechanism.....	4
Figure 4. Displacement versus applied load.....	4
Figure 5. Testbed assembly .....	5
Figure 6. Shaft and clamp connection .....	6
Figure 7. Inner gimbal threads .....	6
Figure 8. Applied torque versus displacement for constant diameter shafts .....	7
Figure 9. Variable diameter shaft dimensions .....	7
Figure 10. Applied torque versus displacement for multiple diameter shafts.....	8
Figure 11. Constant diameter shaft subjected to a torque of 1 N·mm .....	9
Figure 12. 3 mm constant diameter shaft subjected to 1.7 N load .....	9
Figure 13. Maximum stresses for a 3 mm shaft under 1.7 N load .....	10
Figure 14. Stress analysis setup for a multiple diameter shaft .....	10
Figure 15. Stress distribution: $d_1 = 4$ mm, $d_2 = 1.5$ mm, $\tau = 0.1$ N·mm .....	11
Figure 16. Stress distribution: $d_1 = 4$ mm, $d_2 = 1.5$ mm, $\tau = 0.05$ N·mm .....	11
Figure 17. Stress distribution: $d_1 = 4$ mm, $d_2 = 1.5$ mm, $\tau = 0.02$ N·mm .....	11
Figure 18. Stress distribution: $d_1 = 4$ mm, $d_2 = 2$ mm, $\tau = 0.1$ N·mm .....	12
Figure 19. Stress distribution: $d_1 = 4$ mm, $d_2 = 2$ mm, $\tau = 0.05$ N·mm .....	12
Figure 20. Testbed frequency analysis at mode 1 using a shaft diameter of 3 mm.....	13
Figure 21. Testbed frequency analysis at mode 1 using a shaft diameter of 2 mm.....	14
Figure 22. System's frequency response to impulse.....	15
Figure 23. Gimbal calibration connections .....	16
Figure 24. Yaw-axis calibration setup.....	16
Figure 25. Pitch-axis calibration setup.....	17
Figure 26. Yaw-axis calibration .....	18
Figure 27. Pitch-axis calibration .....	18
Figure 28. Roll-axis calibration .....	19
Figure 29. Flywheel assembly.....	20
Figure 30. Flywheel aligned with the yaw-axis .....	20
Figure 31. Commanded speed profiles .....	22
Figure 32. RPM1 (3937 rpm) profile; left: complete, right: zoomed details.....	22
Figure 33. Gimbal displacement for speed profile RPM_1 (3,937 rpm).....	23
Figure 34. Gimbal displacement for speed profile RPM_2 (4,200 rpm).....	24
Figure 35. Gimbal displacement for speed profile RPM_3 (4,500 rpm).....	25
Figure 36. Gimbal displacement for speed profile RPM_4 (5,000 rpm).....	26
Figure 37. FFT of displacement .....	26
Figure 38. GUI in development for torque sensor HIL integration .....	27
Figure 39. Details of GUI input panel .....	28

## LIST OF TABLES

Table 1. Stress Analysis results for a variable diameter shaft.....	12
Table 2. Modal analysis for a shaft diameter of 3 mm.....	13
Table 3. Modal analysis for a shaft diameter of 2 mm.....	13
Table 4. Torsional stiffness comparison.....	19
Table 5. Characteristics of the test setup elements.....	21
Table 6. Commanded flywheel speeds .....	21

This page is intentionally left blank.



## 1. SUMMARY

A key activity in ensuring spacecraft mission success is the verification and validation of spacecraft hardware and software components in relevant environments prior to flight. This is an extremely challenging task to be performed on earth due to the 1-g bias that exists. Air bearing based simulators have become the *de facto* approach for performing these tests; however, air bearing based simulators suffer from (1) limited range of motion and (2) inability to operate in a vacuum. Furthermore, air bearing based simulators used for validating ADCS actuators rely on an inferencing of the actuator's torque output rather than direct measurement of the output. The developed 3-axis torque sensor addresses the deficiencies of air bearing based simulators. Specifically, the torque sensor is capable of operations in a vacuum and thus allows for thermal vacuum testing of ADCS actuators. The prototyped torque sensor is scalable and can be integrated into hardware-in-the-loop testbeds to perform day-in-the-life tests of flight hardware.

## 2. INTRODUCTION

Traditionally, verification and validation of spacecraft attitude determination and control system (ADCS) is performed using spherical air bearing simulators which consist of two concentric spherical surfaces. The rotating bearing section and load are supported by a thin film of pressurized gas bounded by the other bearing section [[1]]. The rotating surface has a limited range of motion about the pitch and roll axes of approximately  $\pm 30^\circ$  [[2]], thus rendering simulations of large angle maneuvers impossible. Furthermore, air bearing testbeds do not directly measure the actuator performance, but rather they use an inference approach to quantify torque and jitter from spacecraft motion measurements. Furthermore, the disturbance torques associated with air bearing simulators include torques arising from the testbed platform, the bearing, the environment, and from the test article itself can be significant and sometimes difficult to compensate [[3]]. Additionally, rapid reconfiguration between different spacecraft operational modes may require significant modifications of the testbed setup. These challenges combined with the air bearing simulator inability to operate in vacuum chambers limits the possibility of reproducing the space environment and the accurate testing and verification of attitude control systems (ACS).

The developed testbed for ACS verification and validation overcomes these challenges by directly measuring actuator output torques using highly accurate laser displacement sensors. Furthermore, environmental torques based on the orbital position and spacecraft attitude can be included either through dynamic model or emulated; e.g., the testbed can be operated inside a vacuum chamber to emulate the vacuum of space. Therefore, the testbed can be used to perform day-in-the-life tests as well as characterize the performance of ACS actuators (and sensors). Additionally, rapid reconfiguration of different spacecraft operational modes such as nadir pointing, sun pointing, orbital maneuvers can be performed quickly by dynamically switching between the modes. The range of spacecraft motion is unlimited thus permitting continuous large angle maneuvers. Additionally, the development and operational cost are expected to be lower than that of air bearing simulators but this is yet to be proved.

A two-axis torque sensing platform, GATorSense, has been previously developed and tested at the University of Florida to characterize the performance of miniaturized control moment gyroscopes (CMGs). In the previous design, the torques were measured using single torque strain-gauge transducers mounted on each axis of the device. The tests showed a high influence of transducer dynamics on the measured data which could not be filtered [[4],[5]]. The new three-axis design eliminates all strain gauge transducers and uses laser displacement sensors by Keyence whose dynamics are outside the measurement range of interest. These sensors consist of a light emitting and a light receiving element, both contained in the same housing. The emitted light beam hits the target then reflects back to the light receiving element. The sensor measures the change in light quantity caused by the target crossing the optical axis. Almost all kinds of materials are detectable, including glass, metal, plastic and wood [[6]]. This effort is an improvement of the design proposed in [[4]].

### **3. METHODS, ASSUMPTIONS, and PROCEDURES**

#### **3.1. Goals and Objectives**

The goal of this effort was the development of hardware-in-the-loop (HIL) simulator for verification and validation of spacecraft attitude determination and control systems (ADCS). The novel testbed developed in this effort allows direct measurement of actuator output torque in relevant environments (thermal and vacuum), thus providing true validation of the performance of the ADCS.

The developed testbed enables realistic HIL simulations for mission assurance, providing end-to-end evaluation of spacecraft ADCS. The developed torque sensor measures the actuator output, which then becomes an input into a high fidelity virtual model of the spacecraft's six degrees-of-freedom motion. Orbital disturbances, based on the spacecraft's position and attitude are also inputs into the virtual model. The testbed is designed to emulate the end-to-end operations of the spacecraft providing the ability to exercise the spacecraft's software algorithms. A schematic of the effort is shown in Figure 1.

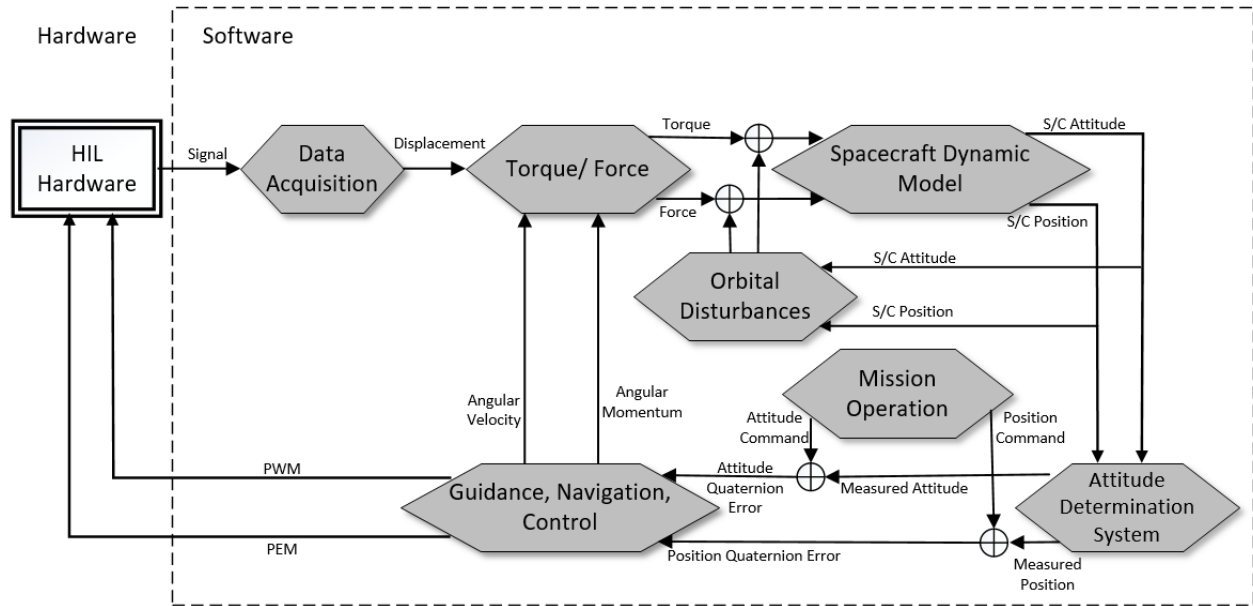


**Figure 1. Schematic of Hardware-in-the-Loop**

### 3.2. Initial Test Mechanism

The primary difference between the current design and the GATorSense design is the use of laser displacement sensors instead of strain gauge transducers. This new approach required calibrated shafts to correlate the displacements of the gimbals to applied torques. A prototype design to assess that the degree of friction in the gimbal and shaft assembly design was fabricated and tested. The prototype consists of a stationary U-bracket with two high precision ball-bearings, a precision shaft, and an emulated gimbal fixed to the shaft via a pin, as shown in Figure 2.

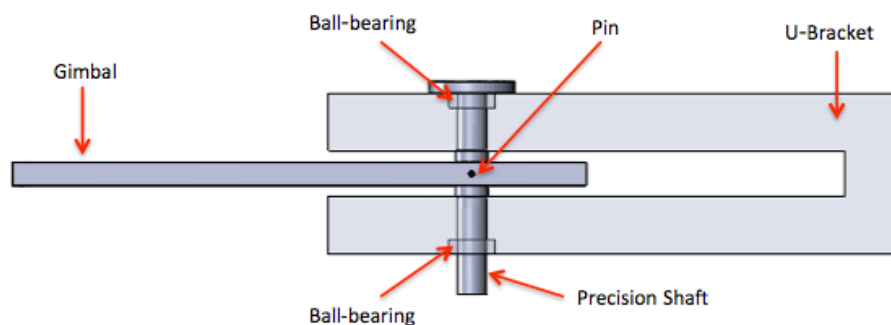


**Figure 2. Schematic of test mechanism assembly**

Loads were applied to the gimbal by attaching different masses at its end as shown in Figure 3. The Keyence laser sensor was used to measure the displacement of the gimbal and Figure 4 shows sample results obtained from this test setup.

The variances shown are attributed primarily to the inability to precisely attach the weights (e.g., different lengths of nylon filaments used to attach the mass to the emulated gimbal).



**Figure 3. Load applied to the test mechanism**

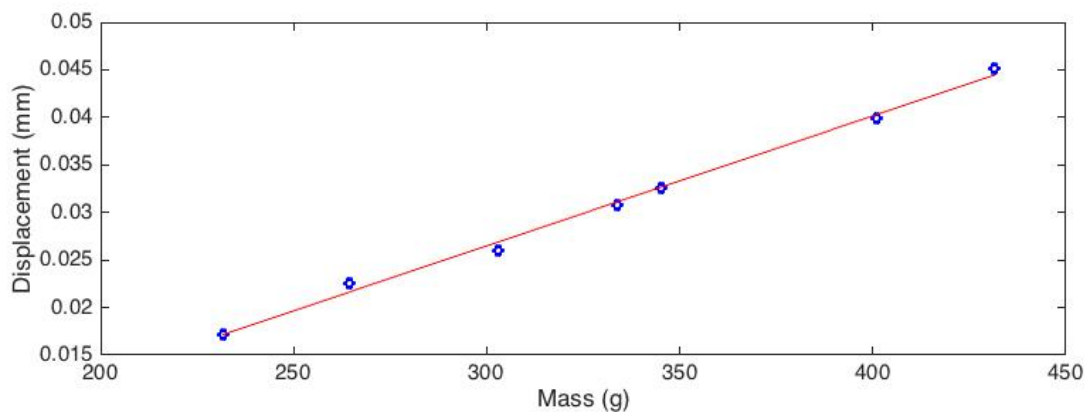


**Figure 4. Displacement versus applied load**

### **3.3. Testbed Development**

The three-axis testbed consists of three mutually orthogonal gimbals as shown in Figure 5. The inner gimbal represents the pitch axis, the intermediate gimbal represents the roll axis and the outer gimbal represents the yaw axis. The pitch axis is pivoted inside the roll axis using four high precision ball bearings, two precision shafts and associated shaft clamps.

One end of the precision shaft is directly attached to the pitch axis gimbal at its inner midpoint, while the other end of the shaft is capsuled inside a shaft clamp that is attached at the outer midpoint of the roll axis gimbal; the shaft clamp connection is shown in Figure 6. Each precision shaft is supported between two precision ball-bearings, one embedded in each gimbal, in order to achieve a near frictionless displacement.

Similarly, the roll axis is pivoted inside the yaw axis, and the yaw axis is pivoted inside the stationary C-Bracket. The C-Bracket is fixed to a reaction mass table with adjustable fine pitch leveling mounts.

The inner gimbal is sized to fit a 1U-sized actuator (i.e., 10x10x10 cm). To accommodate fixturing of the test actuator, the pitch gimbal has sixteen threaded holes as shown in Figure 7. After fixturing the actuator, the static bias (i.e., the center of mass offset) can be counter balanced with the use of a Vernier pitch screw or by subtracting the bias from the measurement. To date, the subtraction of the bias has been the implemented approach.

Each gimbal's displacements are measured using a Keyence H008W laser displacement sensor which are mounted to the reaction table. The measure small linear displacements were converted to angular displacements and then to measured torque. Thus, the need for calibrated shafts.

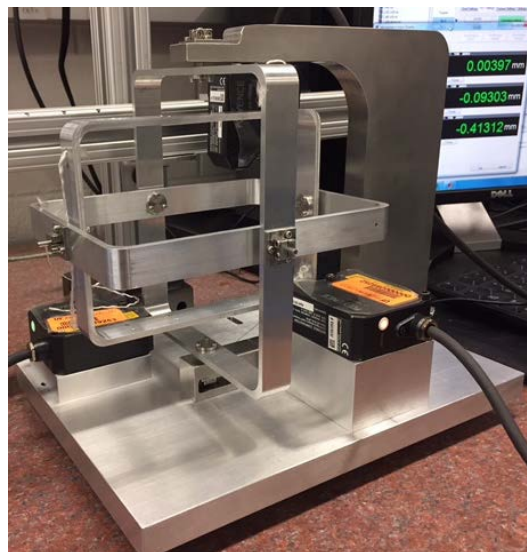


**Figure 5. Testbed assembly**

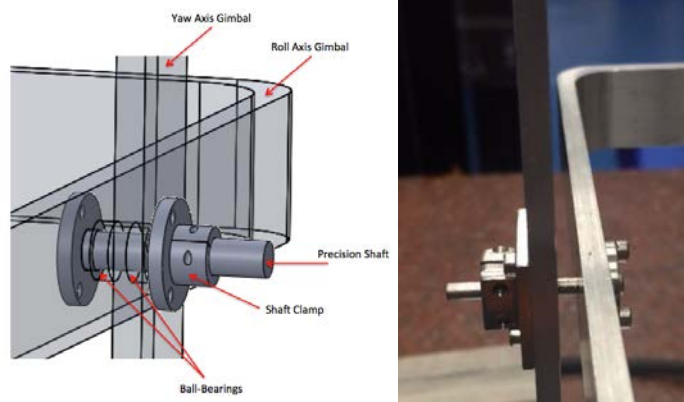


**Figure 6. Shaft and clamp connection**

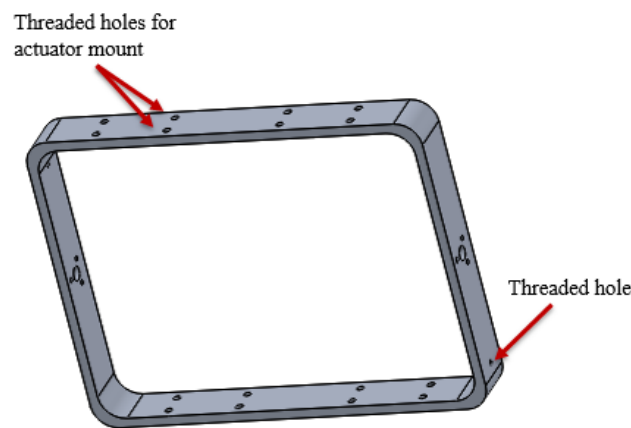


**Figure 7. Inner gimbal threads**

### **3.3.1. Precision Shaft Diameter Selection**

Two precision shaft configurations were investigated: a constant diameter shaft and a multiple diameter shaft. Displacements versus torque curves were developed and compared for both shaft designs. A stress analysis was also conducted to ensure structural integrity under expected loads. From a sensitivity perspective, the final shaft design was selected based on the minimum readable displacement for an applied torque characterizing jitter.

#### Displacement versus torque for a constant diameter shaft

The measured linear displacement  $\delta$  is related to the applied torque by Eq. (1) where  $\tau$  is the applied torque,  $L_s$  is the distance between the pivot point and the measurement point, and  $k$  is the torsional stiffness of the shaft. The torsional stiffness is obtained from using Eq.(2), where  $G$  is the modulus of rigidity,  $J$  is the polar moment of area of the shaft, and  $L$  is the twist length. For stainless steel (SS 316) shafts,  $G = 70$  GPa.

$$\delta = \frac{\tau L_s}{k} \quad (1)$$

$$k = \frac{GJ}{L} = \frac{G\pi d^4}{32L} \quad (2)$$

Three (3) shaft diameters were evaluated:  $d = 4$  mm, 3 mm, 2 mm . For each shaft, the twist length was  $L = 11$  mm and the measurement distance was  $L_s = 74$  mm . The computed stiffness were  $k = 1.6 \times 10^5$  N·mm/rad for the 4 mm shaft,  $k = 5.06 \times 10^4$  N·mm/rad for the 3 mm shaft, and  $k = 1.0 \times 10^4$  N·mm/rad for the 2 mm shaft. Figure 8 shows the displacement with respect to the applied torque for the three considered diameters.

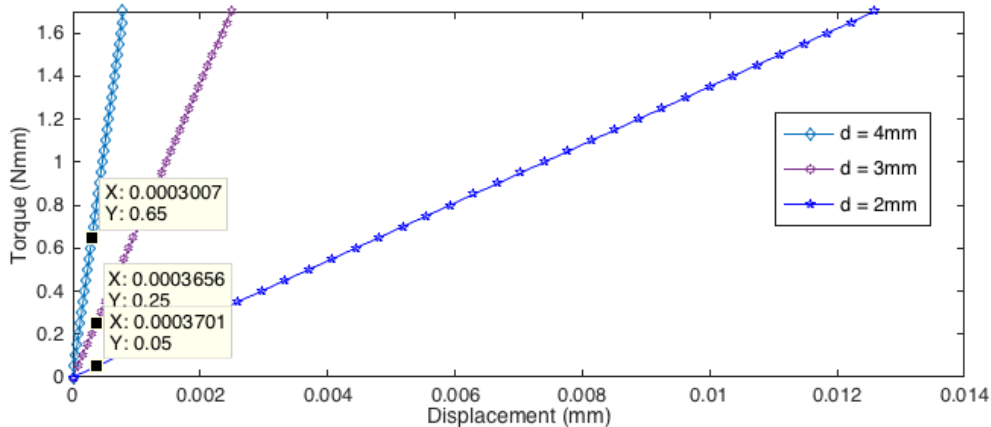


**Figure 8. Applied torque versus displacement for constant diameter shafts**

#### Displacement versus torque for a multiple diameter shaft

For the multiple diameter shafts, the twist length was maintained at  $L = 11$  mm (torque applied 3 mm to the rightmost fillet) and the distance from the pivot point to the measurement point at  $L_s = 74$  mm . The shaft configuration is as shown in Figure 9; two cases were investigated where a single outer shaft diameter of  $d_1 = 4$  mm was considered and two separate inner diameters of  $d_2 = 2$  mm and  $d_2 = 1.5$  mm were investigated. Since the highest stresses will occur near the discontinuities, the torsional constant is calculated for the smallest diameter of the shaft. The displacement versus applied torques for the two considered inner diameters are shown in Figure 10.

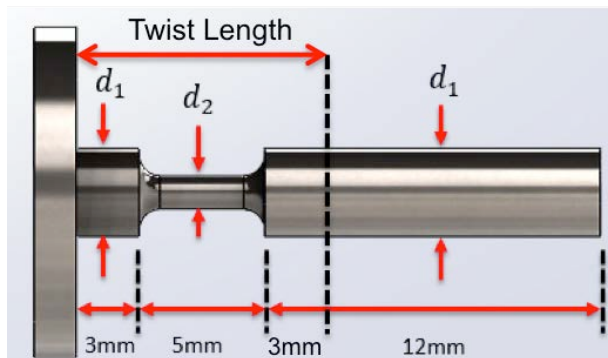


**Figure 9. Variable diameter shaft dimensions**

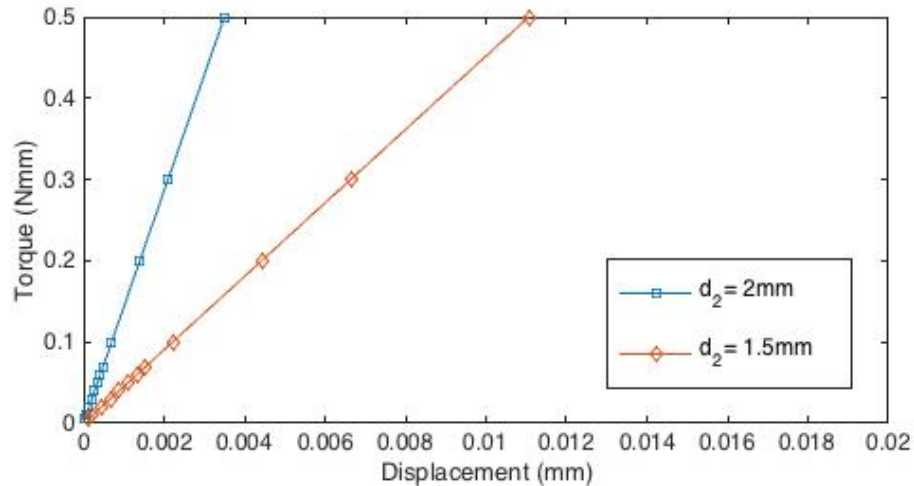


**Figure 10. Applied torque versus displacement for multiple diameter shafts**

#### Sensor Accuracy versus Torque

The Keyence H008W laser displacement sensor has a noted accuracy of 0.0002 mm. Based on the computed stiffness values, the minimum resolvable torque is 0.43 N·mm for the 4 mm shaft, 0.14 N·mm for the 3 mm shaft, and 0.03 N·mm for the 2 mm shaft as shown in Figure 8. For a shaft diameter of 1.5 mm, the minimum resolvable torque is 0.01 N·mm .

### **3.3.2. Testbed Stress Analysis**

#### Constant diameter shaft

A constant diameter, 4 mm, SS 18 shaft was modeled to twist inside two gimbals: the outer gimbal is fixed, and the inner gimbal twists by 1 N·mm . A Von Mises Stress analysis was conducted using SolidWorks and shows a maximum stress of 0.11 MPa (see Figure 11).



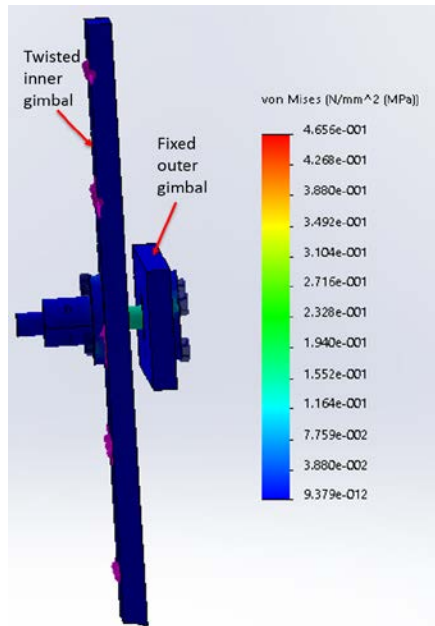


**Figure 11. Constant diameter shaft subjected to a torque of 1 N · mm**

The assembled testbed was subject to a gravity load and an additional load of 1.7 N applied to the inner gimbal to represent a typical actuator. For a shaft diameter of 3 mm, the maximum stress was found to be approximately 2.3 MPa. Figure 13 shows the maximum stresses on the shaft, where the gimbals are hidden in the figure for better viewing of the locations of the maximum stresses.

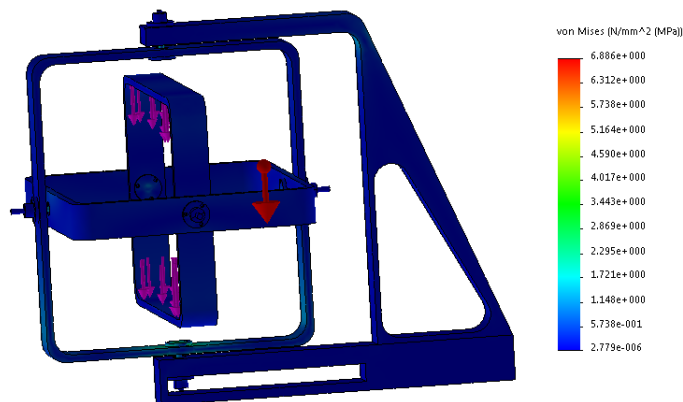


**Figure 12. 3 mm constant diameter shaft subjected to 1.7 N load**

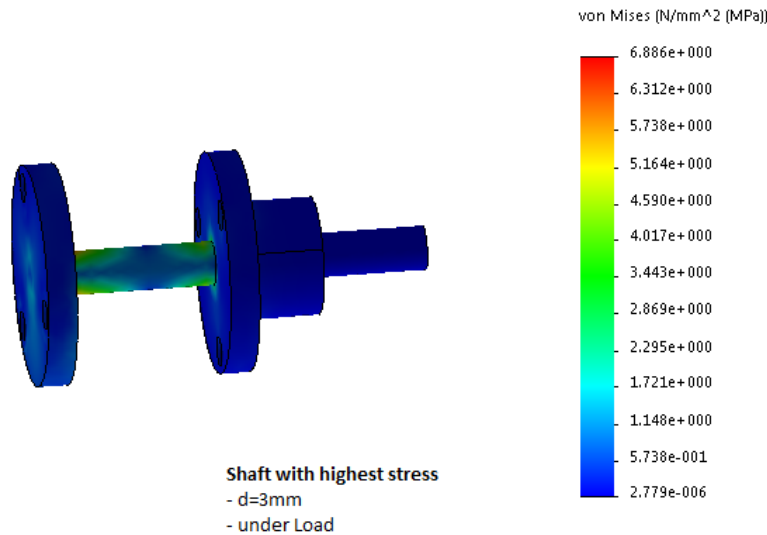


**Figure 13. Maximum stresses for a 3 mm shaft under 1.7 N load**

#### Multiple diameters shaft

Multiple diameter SS 18 shafts were modeled to twist inside two gimbals: the outer gimbal is fixed, and the inner gimbal twists by a specified torque as shown in Figure 14. Each shaft was fixed to the gimbal using a stainless steel clamp. Two configurations were considered; the outer diameter of the shafts were maintained at  $d_1 = 4$  mm and the inner shaft diameters were  $d_2 = 1.5$  mm and  $d_2 = 2$  mm. Von Mises stress analyses were conducted using SolidWorks where the fillet radii of 1 mm were assumed (see Figure 9).

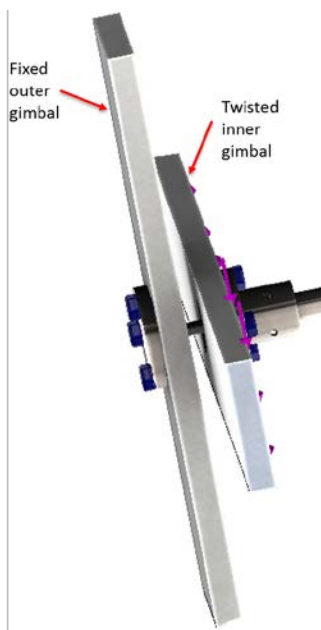


**Figure 14. Stress analysis setup for a multiple diameter shaft**

For each shaft configuration, three loading scenarios were analyzed: applied torques equal to 0.1 N·mm, 0.05 N·mm, and 0.02 N·mm. The results for the shaft with

$d_2 = 1.5$  mm are shown in Figure 15 through Figure 17 and those for  $d_2 = 2.0$  mm are shown in Figure 18 and Figure 19. The gimbals and clamp are hidden in all the figures to better show the stress distribution on the shaft.

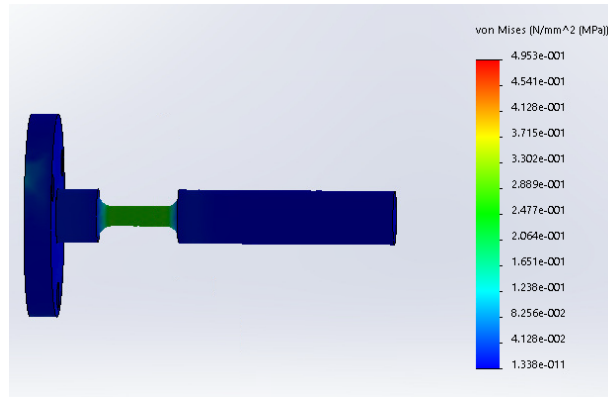


**Figure 15. Stress distribution:**  $d_1 = 4$  mm,  $d_2 = 1.5$  mm,  $\tau = 0.1$  N·mm

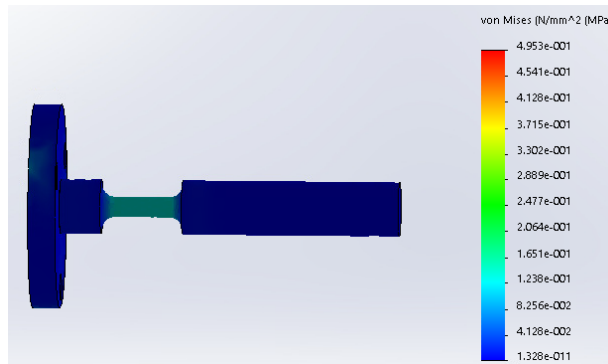


**Figure 16. Stress distribution:**  $d_1 = 4$  mm,  $d_2 = 1.5$  mm,  $\tau = 0.05$  N·mm



**Figure 17. Stress distribution:**  $d_1 = 4$  mm,  $d_2 = 1.5$  mm,  $\tau = 0.02$  N·mm

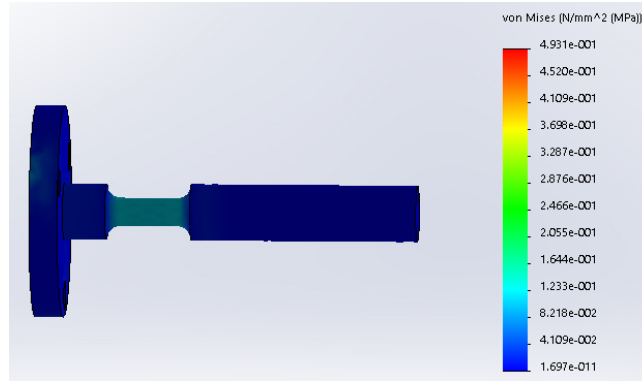


**Figure 18. Stress distribution:**  $d_1 = 4$  mm,  $d_2 = 2$  mm,  $\tau = 0.1$  N·mm

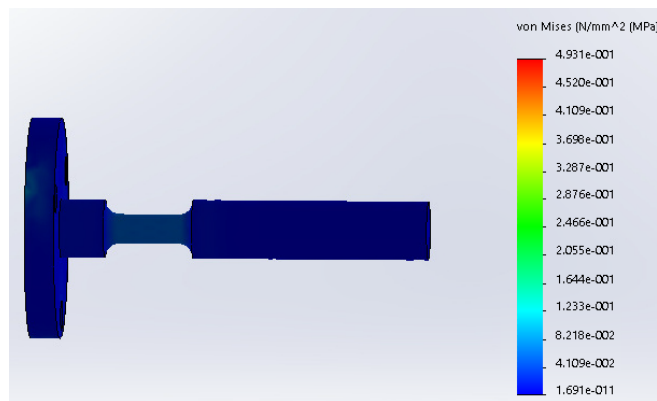


**Figure 19. Stress distribution:**  $d_1 = 4$  mm,  $d_2 = 2$  mm,  $\tau = 0.05$  N·mm

Results for the case  $d_1 = 4$  mm,  $d_2 = 2$  mm,  $\tau = 0.02$  N·mm were not obtained since they represent a case outside the resolvable displacement range.

Table 1 summarizes the results from the SolidWorks stress analysis.

**Table 1. Stress Analysis results for a variable diameter shaft**

Shaft parameters	$\tau = 0.1$ N·mm	$\tau = 0.05$ N·mm	$\tau = 0.02$ N·mm
$d_1 = 4$ mm, $d_2 = 1.5$ mm	0.28 MPa	0.16 MPa	0.03 MPa
$d_1 = 4$ mm, $d_2 = 2$ mm	0.16 MPa	0.08 MPa	-

A 3 mm constant diameter shaft would be better suited for characterizing larger actuators with a higher torque range. The variable diameter shaft was initially considered for characterizing smaller actuators, however, the 1.5 mm shaft experiences approximately double the stress compared to a 2 mm shaft under the same load. Furthermore, for ease of fabrication, a continuous 2 mm shaft diameter was chosen over a varying diameter.

Both the 2 mm and 3 mm continuous diameter shafts were fabricated and the testbed was initially assembled using the 3 mm shafts. The measured data shown later in this report corresponds to the 3 mm diameter shafts.

### 3.4. Testbed Frequency Analysis

A modal analysis was conducted using SolidWorks to estimate the dynamic response of the testbed gimbal assembly for the chosen shaft diameters. Two cases were investigated, a 3 mm constant diameter shaft and a 2 mm constant diameter shaft. The modal analysis results for the 3 mm diameter shaft are shown in Table 2 and Figure 20. Similarly, the modal analysis results for the 2 mm diameter shaft are shown in Table 3, and Figure 21.

**Table 2. Modal analysis for a shaft diameter of 3 mm**

Mode No.	Frequency (rad/s)	Frequency (Hz)	Period (sec)
1	169.33	26.95	0.037
2	247.38	39.37	0.025
3	509.8	81.14	0.012

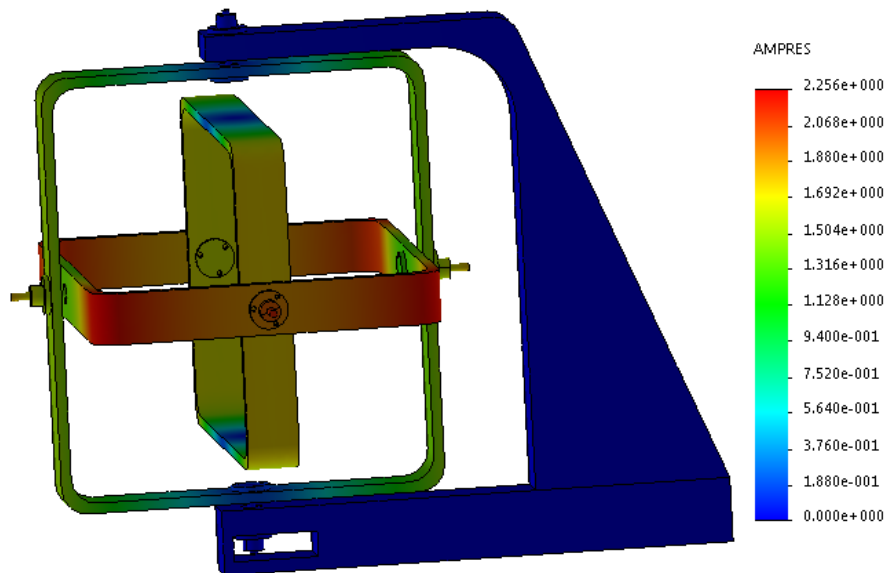


**Figure 20. Testbed frequency analysis at mode 1 using a shaft diameter of 3 mm**

**Table 3. Modal analysis for a shaft diameter of 2 mm**

Mode No.	Frequency (rad/s)	Frequency (Hz)	Period (sec)
1	77.58	12.35	0.081
2	113.64	18.09	0.055
3	242.96	38.67	0.026

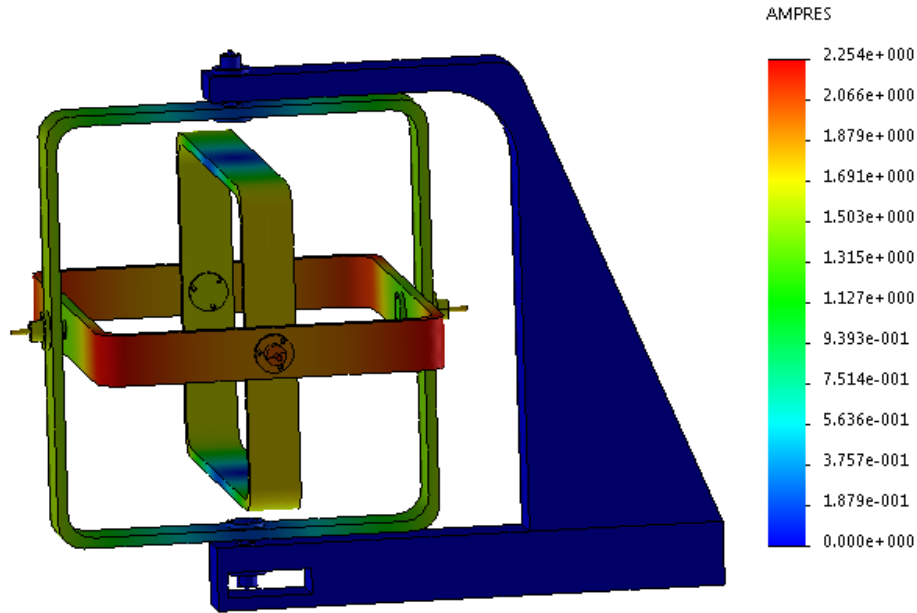


**Figure 21. Testbed frequency analysis at mode 1 using a shaft diameter of 2 mm**

The simulated modal analysis shows the frequency at the first three modes for the two considered shaft diameters. For a shaft diameter of 3 mm, the testbed has a first natural mode of 26.95 Hz, and for a shaft diameter of 2 mm, the first natural mode is 12.35 Hz.

### 3.5. Testbed Frequency Test

The testbed was assembled using 3 mm precision shafts and an impulse was applied to the outer gimbal. The system's frequency response shown in Figure 22 and good correlation with the analytical results (Table 2) is observed. Observed differences are attributable to unmodelled components in the analytical model; e.g., the bearings were not included in the analytical models and although they were preloaded during assembly, they do contribute to the system's response.

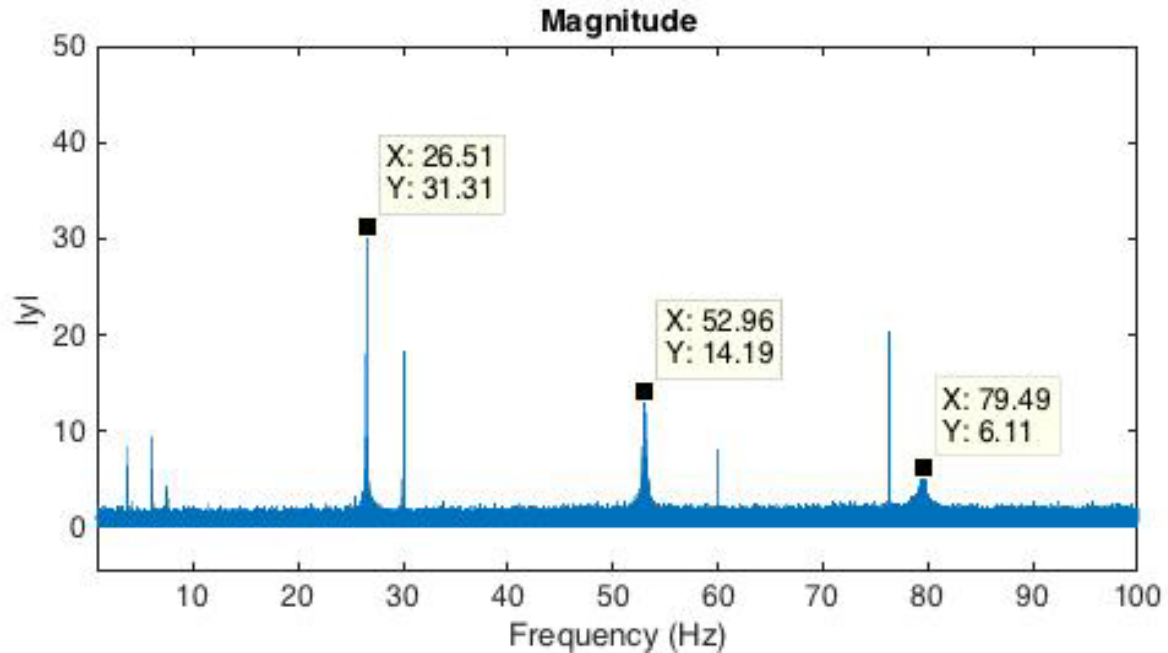


**Figure 22. System's frequency response to impulse**

### **3.6. Testbed Calibration**

Calibration of the testbed commenced once the testbed was fully assembled. The analog displacement signals from all three (3) Keyence LK-H008W laser sensors were conditioned using the Keyence LK-G5001 sensor controller. The conditioned analog displacement output signals from the LK-G5001 controller were read using National Instruments (NI) USB-6221 BNC data acquisition (DAQ) system sampled at 1000 Hz (to be consistent with the Simulink model simulation model). The calibration process is as outlined below.

#### **3.6.1. Calibration process**

For the yaw gimbal (i.e., outer gimbal):

- The initial position of each gimbal was measured before applying a load (i.e., unloaded static position)
- The gimbal was connected to a turnbuckle, which in turn was connected to a load cell (Interface WMCP-1000G) through an adapter. The opposite end of the load cell was connected to a fixed rail wall. All connections are tight. The connections are shown in Figure 23.
- Various loads were applied to the gimbal by adjusting the turnbuckle. For example, the load is applied at the threaded hole, at the right side of the yaw-axis gimbal, shown in Figure 24.
- The applied loads were recorded and for every applied load the displacement was measured using the Keyence sensor.
- The displacement versus load plots were generated and the measured torsional stiffness  $k$  was calculated from Eq. (3).

$$\tau = k \frac{\delta}{L_S} = \frac{F L_A}{L_S} \Rightarrow k = \frac{F}{\delta} L_S L_A \quad (3)$$

$\underbrace{\delta}_{\text{measured}}$ 
 $\underbrace{F}_{\text{applied}}$

where  $\delta$  is the gimbal displacement measured with the Keyence sensor,  $L_S$  is the distance from the pivot point to the measurement point,  $F$  is the applied load read from the load cell, and  $L_A$  is the distance from the pivot point to the load application point.

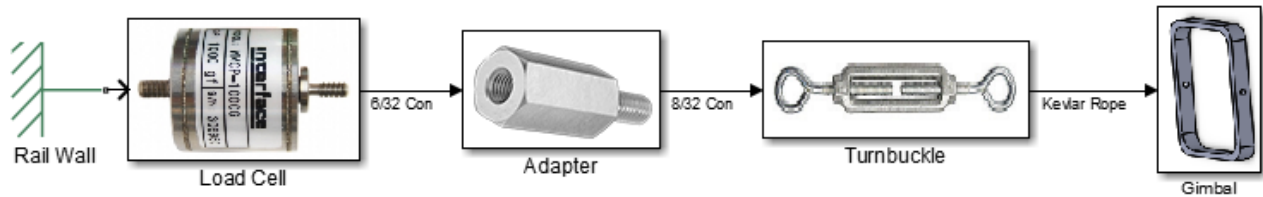


**Figure 23. Gimbal calibration connections**

The process was repeated for the inner (i.e., pitch and roll) gimbal with these additional steps:

- A load was applied in the opposite directions to generate a couple (i.e., pure torque) and minimize displacement of the other gimbals. To accomplish this, another turnbuckle (Turnbuckle 2) was attached to the opposite end of the gimbal; Turnbuckle 2 was attached to a fixed rail wall.
- The calibration process was repeated, while simultaneously assuring that the outer gimbal was at its initial position; this was accomplished by measuring the gimbal displacement and adjusting the opposing load.

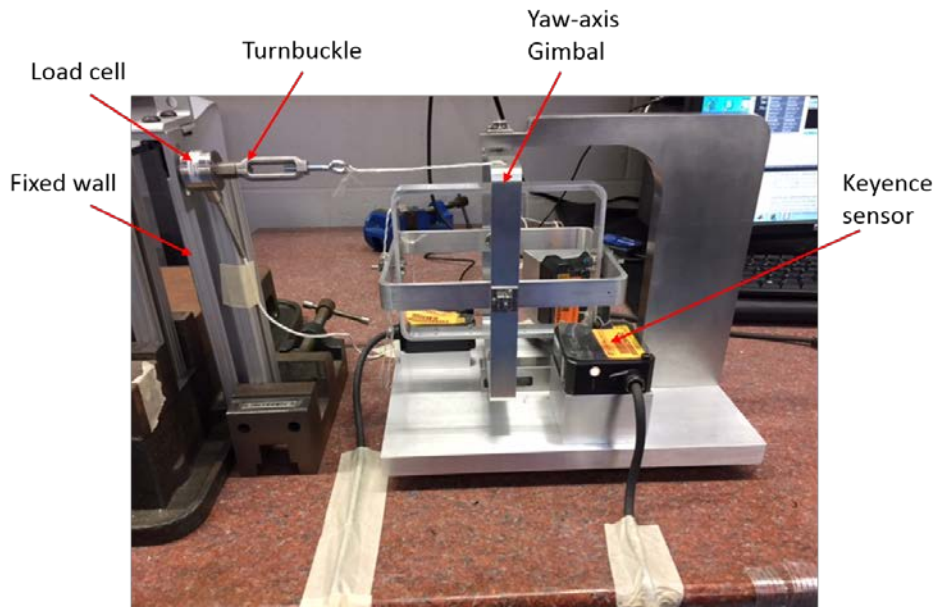


**Figure 24. Yaw-axis calibration setup**



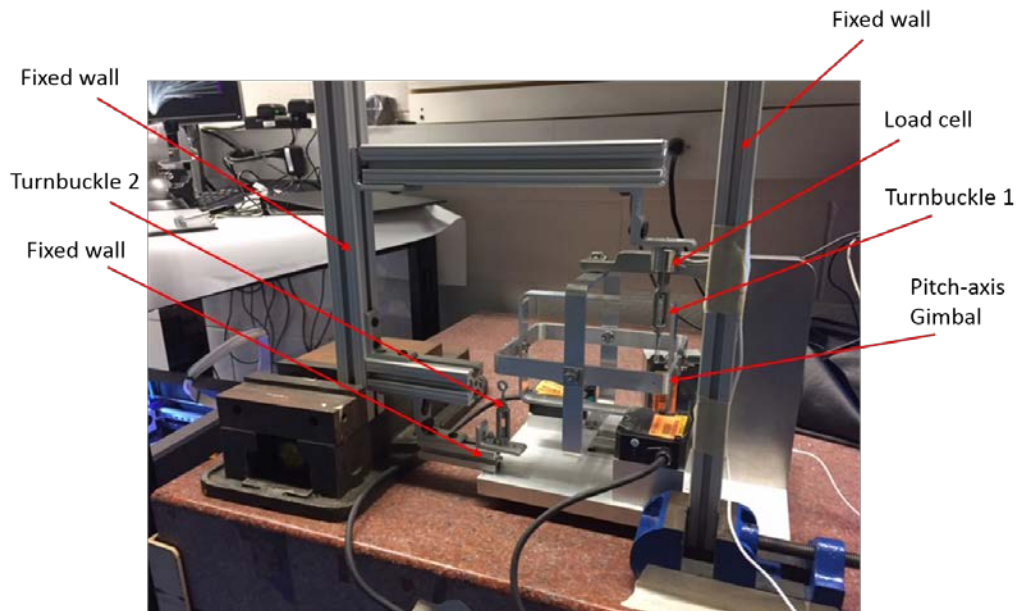


**Figure 25. Pitch-axis calibration setup**

### Lessons Learned

The calibration was challenging because it required precise alignment of the turnbuckle(s) perpendicular to the axis of rotation. A single turnbuckle equipped with a load cell was used on the yaw axis since a pure torque was not mandatory (interior gimbals not affected by motion of outer gimbal). However, the pitch and roll axes required two turnbuckles to produce a pure torque and thus were a bit more challenging since ensuring that both turnbuckles lie on the same plane was critical. Furthermore, adjusting the turnbuckles until the loads were accurately balanced was difficult. In order to minimize the dynamics of the turnbuckle mechanism on the measurements, one end of the turnbuckle must be fixed to the rail walls in order to avoid noisy measurements.

### **3.6.2. Calibration Results**

Figure 26, Figure 27, and Figure 28 show sample results obtained from the calibration tests. Each measurement point was sampled at 5000 Hz for a duration of 60 second, then the measurements were averaged. The variances shown in the roll and pitch axis calibration are due to manually adjusting the opposing end of the gimbal to ensure a pure torque is applied to the test gimbal; i.e., to ensure no torque is applied to the other gimbals currently not under test. It is worth noting that the Interface load cell used for the tests outputs force in units of *gm-force*, thus the ordinates of these figures are labelled as “mass” but actually are representative of the applied force ( $1 \text{ gm} \Leftrightarrow 1 \text{ gm f} = 0.0098 \text{ N}$ ).

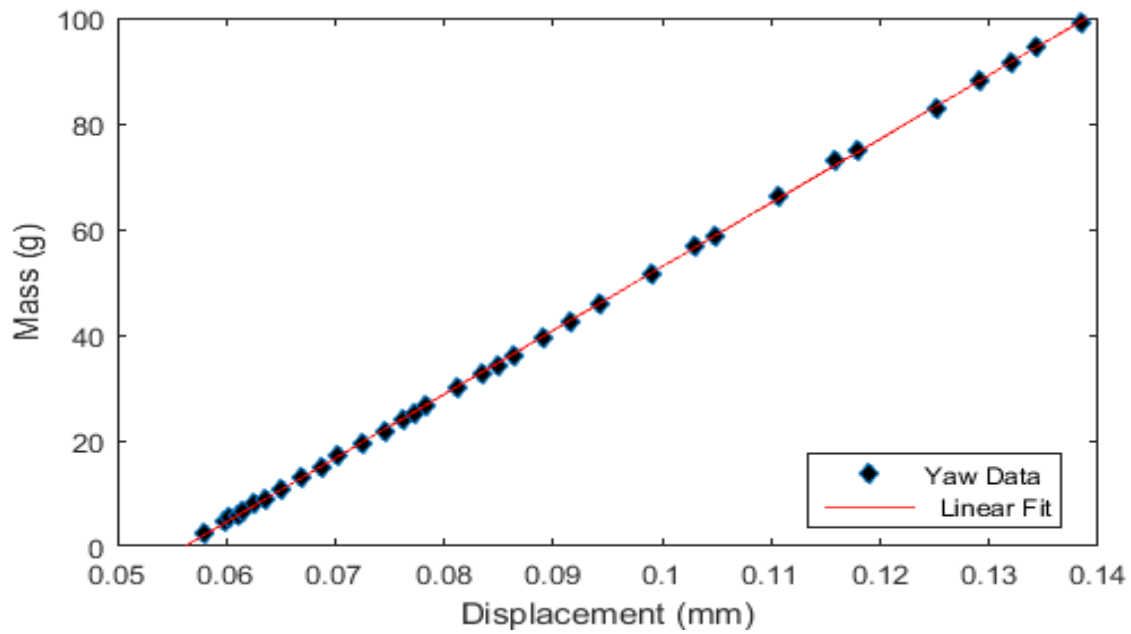


**Figure 26. Yaw-axis calibration**

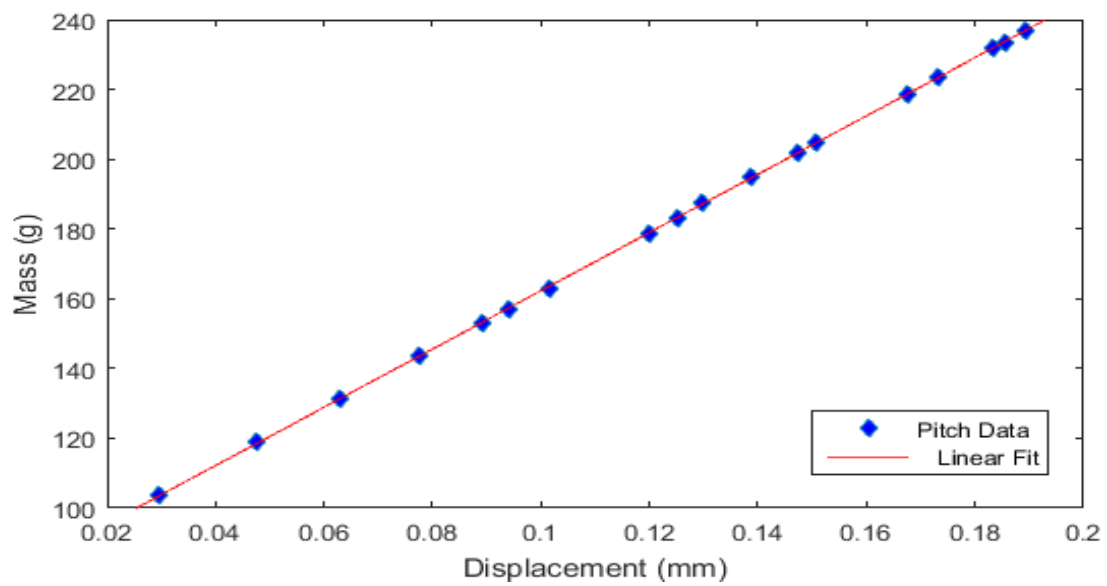


**Figure 27. Pitch-axis calibration**

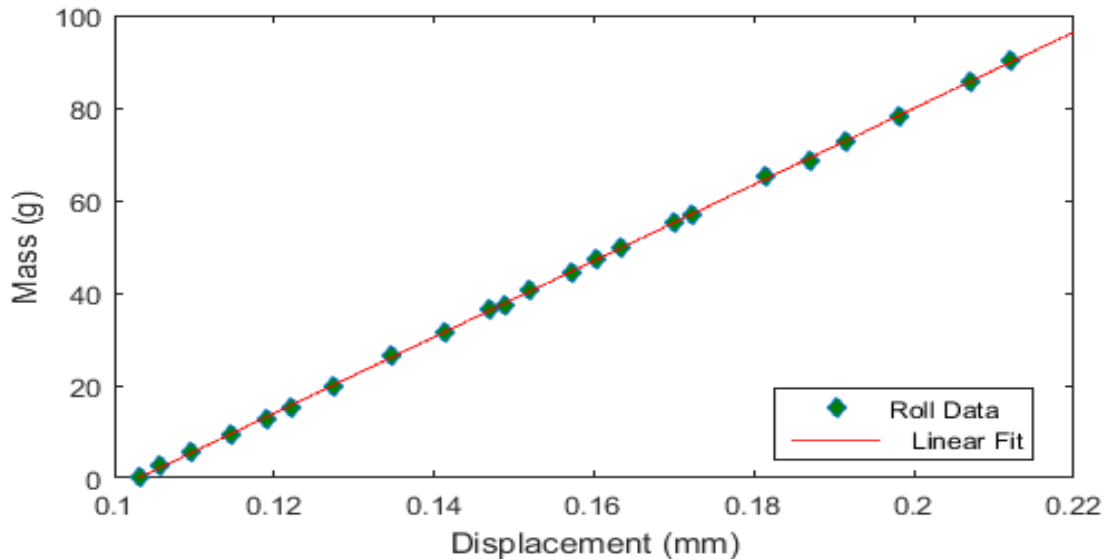


**Figure 28. Roll-axis calibration**

Table 4 shows the calculated torsional stiffness and measured torsional stiffness for each axis. The differences between these quantities are 2.3%, 6.1%, and 5.4% for the roll-axis, pitch-axis, yaw-axis, respectively. These observed differences can be attributed to several factors including (1) material properties (i.e., assumed modulus of rigidity), (2) variations in shaft diameters (i.e., precision during fabrication), (3) twist length of the shaft (i.e., torque application points), (4) load application point and/or direction (i.e., turnbuckles), (5) friction between moving parts, and (6) quality of the overall calibration process (e.g., the use of turnbuckles for load application).

**Table 4. Torsional stiffness comparison**

$k$ (N·mm)	Roll-axis	Pitch-axis	Yaw-axis
<b>Calculated</b>	$5.06 \times 10^4$	$5.06 \times 10^4$	$5.06 \times 10^4$
<b>Measured</b>	$5.18 \times 10^4$	$5.38 \times 10^4$	$5.34 \times 10^4$
<b>Differences (%)</b>	2.3	6.1	5.4

### 3.7. Actuator testing

The actuator under test is an in-house designed/fabricated flywheel assembly shown in Figure 29. It consists of a single double-shafted brushless DC motor, two flywheels, housing, and associated electronics. The device is an early prototype of a flywheel system developed in-house and is used primarily to demonstrate the feasibility of the developed sensor. It is not a precision device and thus itself is very noisy in its operations; e.g., the motor controller electronics is incapable of precisely maintaining the flywheel speed.



**Figure 29. Flywheel assembly**

Prior to mounting the actuator on the testbed, the zero position (balance) was recorded. The flywheel assembly was mounted at the center of the inner gimbal, such that the flywheels are aligned with the yaw-axis. The speed control and measurement unit consists of an Arduino microcontroller, a motor driver and a power supply. The microcontroller provides the set point speed, the motor driver maintains this speed and sends the actual speed to the microcontroller. The Keyence sensors record the displacement of the testbed gimbals as the flywheel speeds are varied. The test setup is shown in Figure 30. Table 5 shows the characteristics of the test elements.

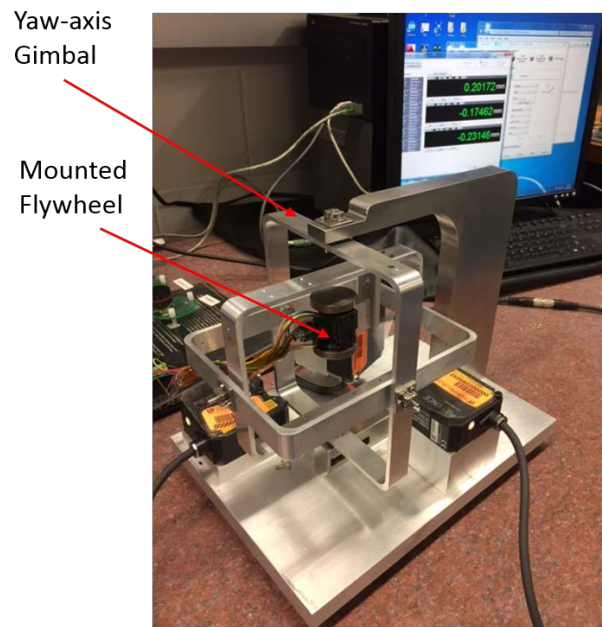


**Figure 30. Flywheel aligned with the yaw-axis**

**Table 5. Characteristics of the test setup elements**

Element	Characteristic	
Torque sensing testbed	Torsional Stiffness	$k_{roll} = 5.18 \times 10^4 \text{ N} \cdot \text{mm}$ $k_{pitch} = 5.38 \times 10^4 \text{ N} \cdot \text{mm}$ $k_{yaw} = 5.34 \times 10^4 \text{ N} \cdot \text{mm}$
Keyence sensor	Model	H008W
	Accuracy	0.0002 mm
Flywheel	Inertia	42 kg · mm <sup>2</sup>
	Motor Model	Faulhaber Series 1628 B
Speed Controller	Faulhaber 2-quadrant PWM - Series SC 2804	
Arduino	Uno	
PC	Data Logging	

The flywheel was commanded to spin from rest for 200 seconds then decelerate to zero. Four different flywheel speeds were commanded and are listed in Table 6 with the associated output profiles shown in Figure 31. RPM\_1 has a rise time of 9 secs, RPM\_2 has a rise time of 8.8 secs, RPM\_3 has a rise time of 9.3 secs and RPM\_4 has a rise time of 9.6 secs. Figure 32 shows the recorded response for the RPM\_1 case showing the inability of the prototype flywheel to precisely maintain its speed. This speed variation is observed in the measured gimbal displacements (i.e., scaled torques). The sharp falloff in speed during the deceleration phase of the flywheel is due to the inability to speed controller specify the motor's fall-time and essentially the deceleration occurs due to the motor being powered off and the flywheel coasting to a stop.

**Table 6. Commanded flywheel speeds**

Profile #	Speed (rpm)
RPM_1	3,937
RPM_2	4,200
RPM_3	4,500
RPM_4	5,000

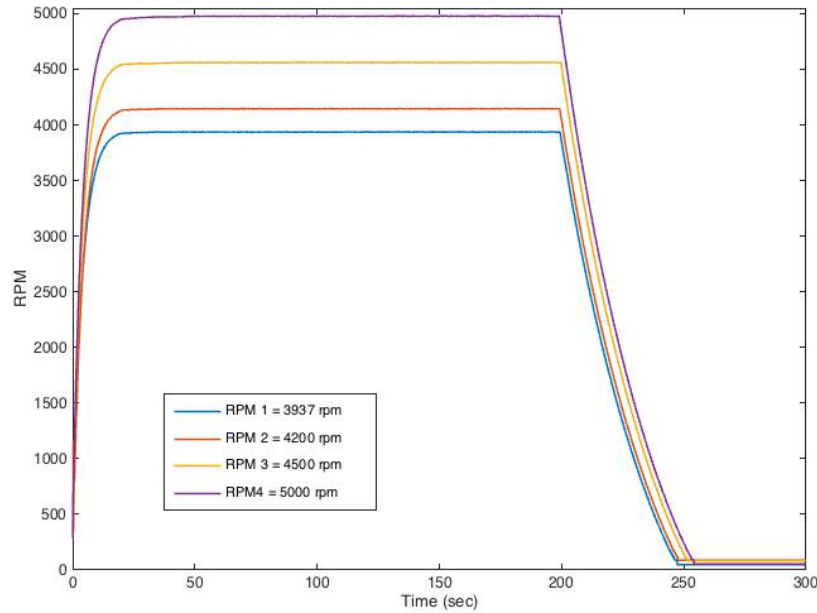


**Figure 31. Commanded speed profiles**

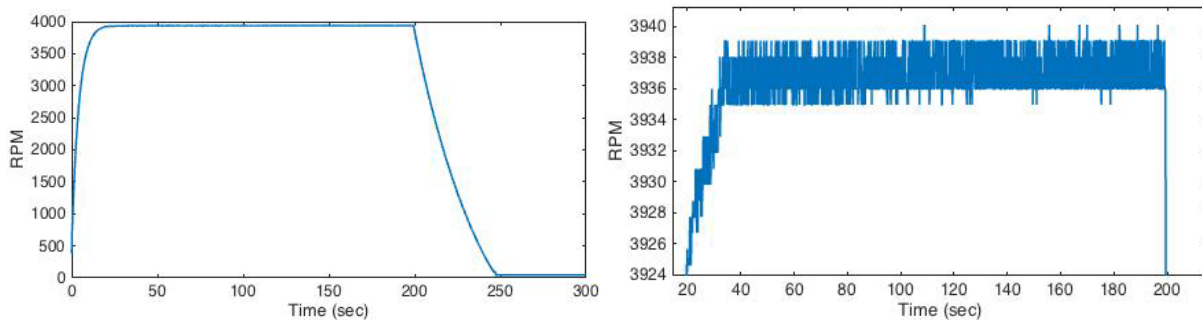


**Figure 32. RPM1 (3937 rpm) profile; left: complete, right: zoomed details**

For the four flywheel speed profiles shown in Table 6, Figure 33 through Figure 36 show displacement (i.e., scaled torque) outputs of each gimbal for a pitch-axis input command. These figures show spin-up torque on the pitch axis as well as the flywheel jitter on the other two axes. The inability of flywheel system to maintain a commanded speed is also demonstrated by the high frequency responses shown in all three axes. Furthermore, as the motor is powered down to decelerate the flywheel, the system passes through its first resonant frequency ( $\sim 1800$  rpm) and shows up as spikes on all three axes. The FFT shown in Figure 37 of the pitch displacement confirms a system resonance at 28.82 Hz (1729 rpm). As stated earlier in section 3.5, further investigations of the bearing preloads are required to move the system's resonance frequencies higher or to dampen the gimbal joints to minimize the effects. A combination of both preload and damping may also be a feasible solution and is also worth investigating.

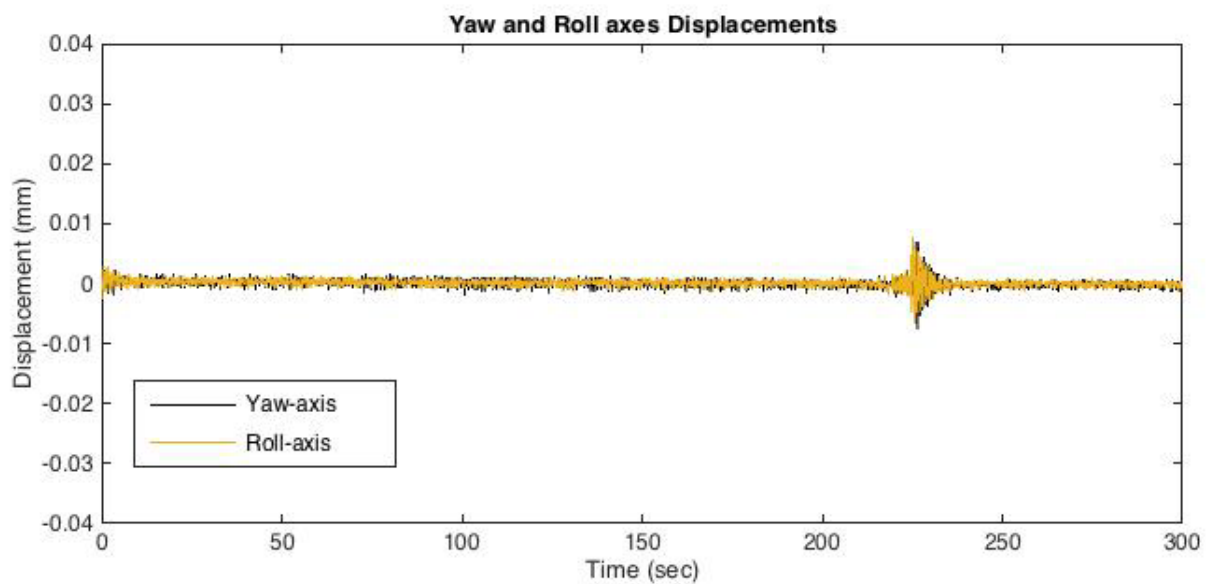
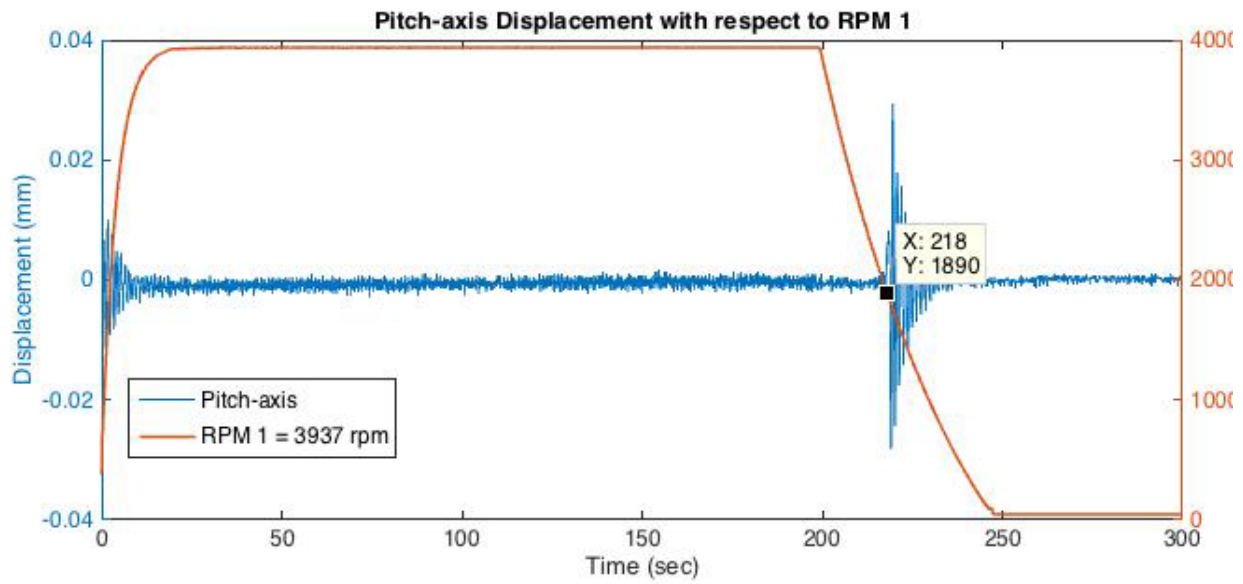


**Figure 33. Gimbal displacement for speed profile RPM\_1 (3,937 rpm)**

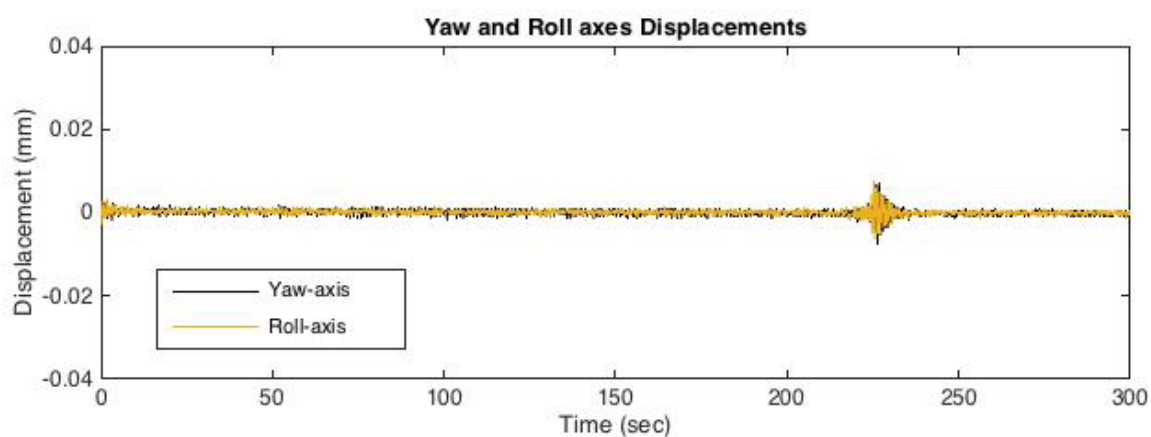
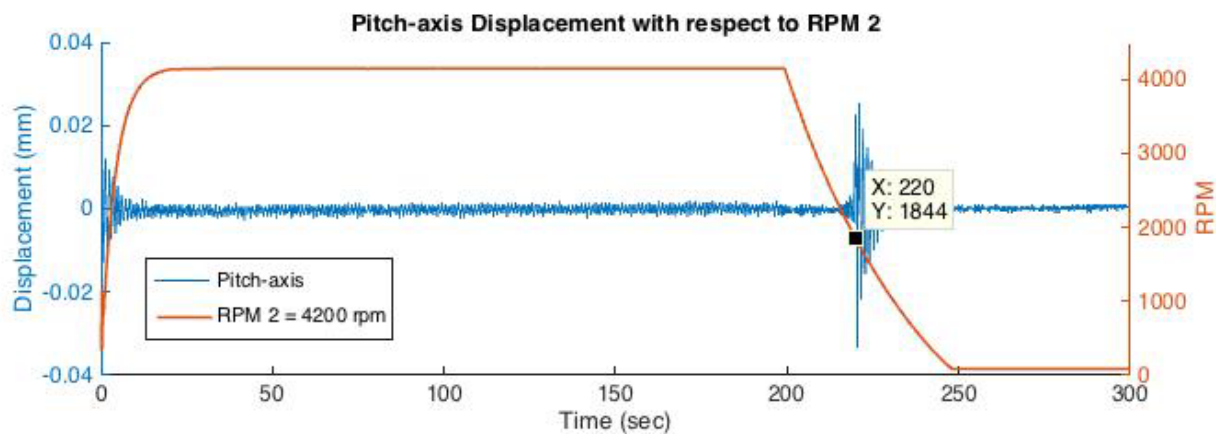


**Figure 34. Gimbal displacement for speed profile RPM\_2 (4,200 rpm)**



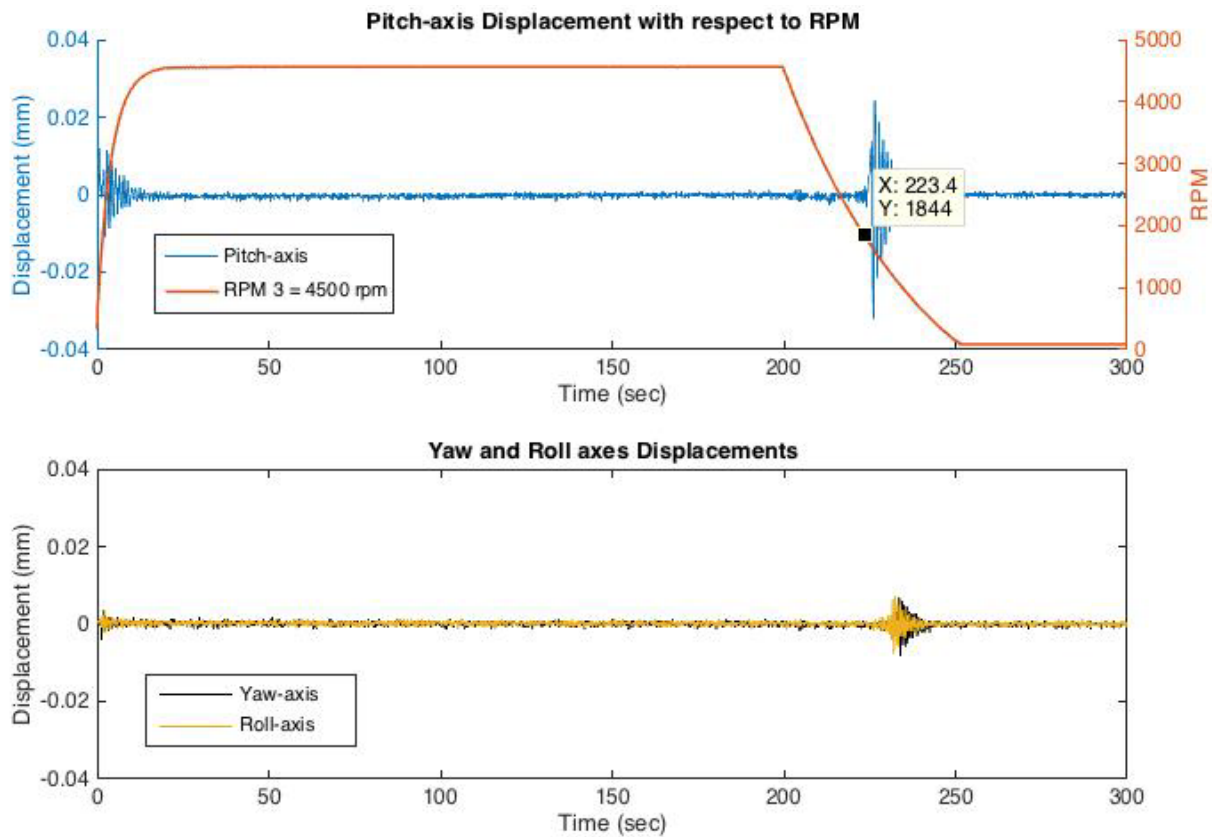


**Figure 35. Gimbal displacement for speed profile RPM\_3 (4,500 rpm)**

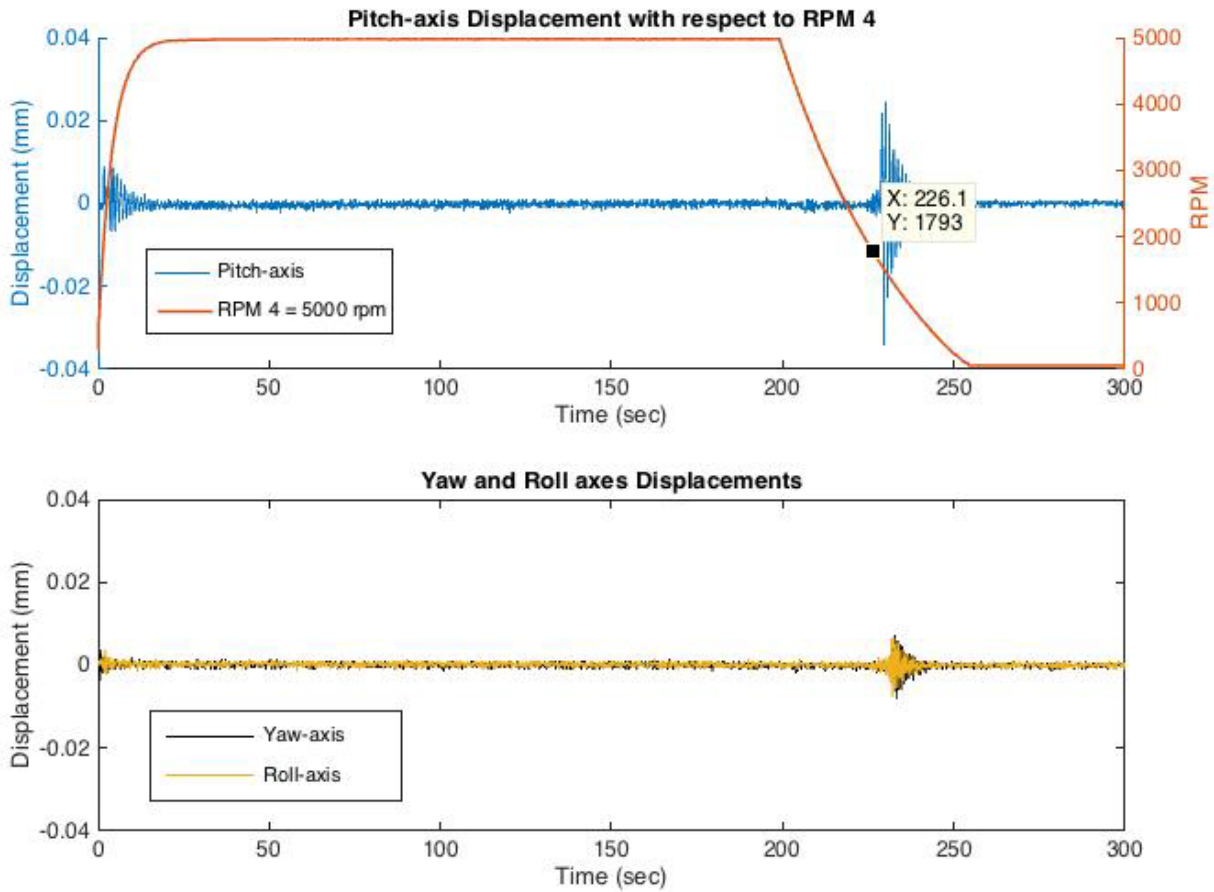


**Figure 36. Gimbal displacement for speed profile RPM\_4 (5,000 rpm)**

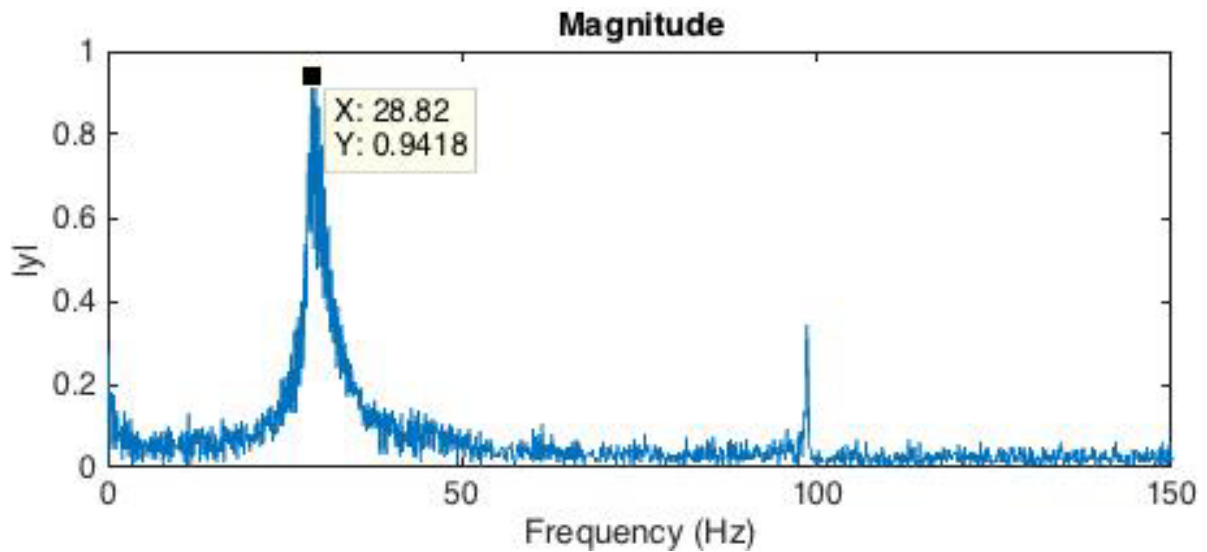


**Figure 37. FFT of displacement**

### 3.8. Graphical User Interface (GUI)

To facilitate the integration of the torque sensor into a hardware-in the loop (HIL) testbeds for simulation of different spacecraft scenarios, a graphical user interface (GUI) is being developed. A preliminary version of the GUI is shown in Figure 38 where the input panel is reproduced in Figure 39 to show the various input parameters. Currently, the input parameters include spacecraft physical characteristics (e.g., mass, centroidal inertial, and physical dimension), attitude actuator options (e.g., CMG, RW, magnetorquer), flywheel characteristics, and flywheel motor characteristics. The intent of this interface is to provide flexibility in use of the sensor yet streamline the input required to utilize the torque sensor in a HIL environment. This is an ongoing activity and results will be published once the effort is significantly mature.

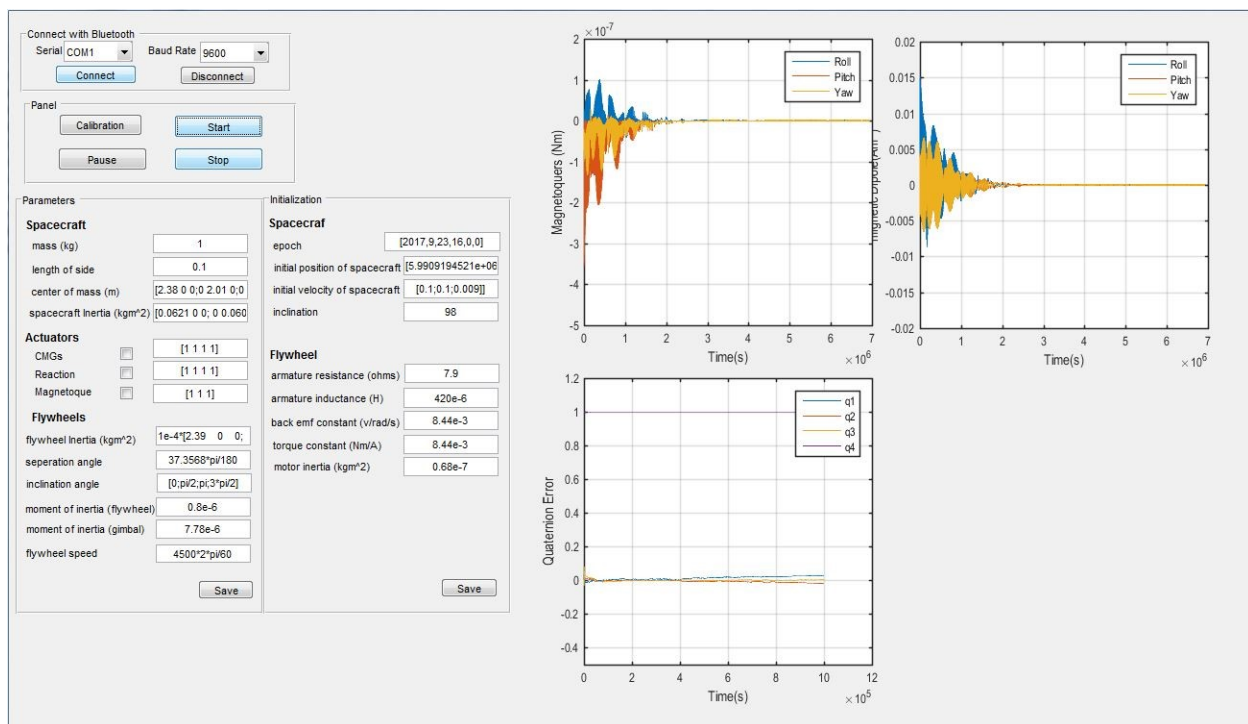


Figure 38. GUI in development for torque sensor HIL integration

Connect with Bluetooth

Serial COM1
Baud Rate 9600

Connect
Disconnect

Panel

Calibration
Start

Pause
Stop

Parameters

Spacecraft

mass (kg) 1
length of side 0.1
center of mass (m) [2.38 0 0; 0 2.01 0; 0]
spacecraft inertia (kgm<sup>2</sup>) [0.0621 0 0; 0 0.060]

Actuators

CMGs ☐ [1 1 1 1]
Reaction ☐ [1 1 1 1]
Magnetorque ☐ [1 1 1]

Flywheels

flywheel inertia (kgm<sup>2</sup>) 1e-4\*[2.39 0 0; 0 0 0]
seperation angle 37.3568\*pi/180
inclination angle [0;pi/2;pi;3\*pi/2]
moment of inertia (flywheel) 0.8e-6
moment of inertia (gimbal) 7.78e-6
flywheel speed 4500\*2\*pi/60

Save

Initialization

Spacecraf

epoch [2017,9,23,16,0,0]
initial position of spacecraft [5.9909194521e+06]
initial velocity of spacecraft [0.1;0.1;0.009]
inclination 98

Flywheel

armature resistance (ohms) 7.9
armature inductance (H) 420e-6
back emf constant (v/rad/s) 8.44e-3
torque constant (Nm/A) 8.44e-3
motor inertia (kgm<sup>2</sup>) 0.68e-7

Save

Figure 39. Details of GUI input panel

28

Approved for public release; distribution is unlimited

## 4. CONCLUSION

A key activity in ensuring spacecraft mission success is the verification and validation of spacecraft hardware and software components in relevant environments prior to flight. This is an extremely challenging task to be performed on earth due to the 1-g bias that exists. Air bearing based simulators have become the *de facto* approach for performing these tests; however, air bearing based simulators suffer from (1) limited range of motion and (2) inability to operate in a vacuum. Furthermore, air bearing based simulators used for validating ADCS actuators rely on an inferencing of the actuator's torque output rather than direct measurement of the output. The developed 3-axis torque sensor addresses the deficiencies of air bearing based simulators. Specifically, the torque sensor is capable of operations in a vacuum and thus allows for thermal vacuum testing of ADCS actuators.

The prototyped torque sensor is scalable and can be integrated into hardware-in-the-loop testbeds to perform day-in-the-life tests of flight hardware. Future activities include (1) addressing the gimbals to increase the system's resonant frequency, (2) completion of the GUI, (3) integration of a wireless interface to eliminate cabling across the testbed, (4) integration of an onboard power supply (batteries) to eliminate cabling across the testbed, (5) addition testing to validate the performance of the system.

## REFERENCES

- [1] Jana L., Schwartz, Mason A., Peck, and Christopher D. Hall, "Historical Review of Air-Bearing Spacecraft Simulators," *Journal of Guidance, Control and Dynamics*, vol. 26, no. 4, pp. 513-522, 2003.
- [2] D., Tsiotras, P., Jung, "A 3-DoF Experimental Test-Bed for Integrated Attitude Dynamics and Control Research," in *AIAA*, Austin, Texas, p. 5331, 2003.
- [3] Allen G., Smith, "Dynamic Simulators for Test of Space Vehicle Attitude Control Systems," in *Proceedings of the Conference on the Role of Simulation in Space Technology, Part C, Virginia Polytechnic Inst. & State University*, Blacksburg, VA, 1964.
- [4] V., Nagabhushan and N., Fitz-Coy, "Scalable, HIL, Unconstrained 3-Axis Test Bed for Attitude Control System," in *AAS Astrodynamics Specialist Conference*, Toronto, Ontario, Canada, 2010.
- [5] S., Allgeier, N., Fitz-Coy, and V., Nagabhushan, "Architecture For Unconstrained 3-Axis Attitude Determination and Control Test Bed," in *AAS*, 2011.
- [6] "Measurement Sensors," KEYENCE America, [Online]. Available: <http://www.keyence.com/products/measure/index.jsp>. Accessed 23 March 2018.

## DISTRIBUTION LIST

DTIC/OCF

8725 John J. Kingman Rd, Suite 0944

Ft Belvoir, VA 22060-6218

1 cy

AFRL/RVIL

Kirtland AFB, NM 87117-5776

1 cy

Official Record Copy

AFRL/RVES/Josue Munoz

1 cy

This page is intentionally left blank.